



Article

Facile Synthesis of Microporous Carbons from Biomass Waste as High Performance Supports for Dehydrogenation of Formic Acid

Tingting Cao^{1,2,†}, Jinke Cheng^{1,2,†}, Jun Ma^{1,2}, Chunliang Yang^{1,2}, Mengqin Yao^{1,2,*}, Fei Liu^{1,2,*}, Min Deng^{1,2}, Xiaodan Wang^{1,2} and Yuan Ren^{2,*}

¹ School of Chemistry and Chemical Engineering, Guizhou University, Guiyang 550025, China; caotingting980417@163.com (T.C.); jkcheng@gzu.edu.cn (J.C.); jma3@gzu.edu.cn (J.M.); clyang@gzu.edu.cn (C.Y.); gzu403299473@163.com (M.D.); wangxiaodan0516@126.com (X.W.)

² Key Laboratory of Green Chemical and Clean Energy Technology, Guizhou University, Guiyang 550025, China

* Correspondence: mqyao@gzu.edu.cn (M.Y.); ce.feiliu@gzu.edu.cn (F.L.); renyuan_1986@126.com (Y.R.)

† These two authors contributed equally to this work.

Abstract: Formic acid (FA) is found to be a potential candidate for the storage of hydrogen. For dehydrogenation of FA, the supports of our catalysts were acquired by conducting ZnCl₂ treatment and carbonation for biomass waste. The texture and surface properties significantly affected the size and dispersion of Pd and its interaction with the support so as to cause the superior catalytic performance of catalysts. Microporous carbon obtained by carbonization of ZnCl₂ activated peanut shells (C_{PS}-ZnCl₂) possessing surface areas of 629 m²·g⁻¹ and a micropore rate of 73.5%. For ZnCl₂ activated melon seed (C_{MS}-ZnCl₂), the surface area and micropore rate increased to 1081 m²·g⁻¹ and 80.0%, respectively. In addition, the introduction of ZnCl₂ also caused the increase in surface O content and reduced the acidity of the catalyst. The results represented that C_{MS}-ZnCl₂ with uniform honeycomb morphology displayed the best properties, and the as-prepared Pd/C_{MS}-ZnCl₂ catalyst afforded 100% hydrogen selectivity as well as excellent catalytic activity with an initial high turnover number (TON) value of 28.3 at 30 °C and 100.1 at 60 °C.

Keywords: porous carbon; Pd nano-catalysts; agriculture waste; formic acid; dehydrogenation



Citation: Cao, T.; Cheng, J.; Ma, J.; Yang, C.; Yao, M.; Liu, F.; Deng, M.; Wang, X.; Ren, Y. Facile Synthesis of Microporous Carbons from Biomass Waste as High Performance Supports for Dehydrogenation of Formic Acid. *Nanomaterials* **2021**, *11*, 3028. <https://doi.org/10.3390/nano11113028>

Academic Editors: Jiabiao Lian and Goran Drazic

Received: 16 October 2021

Accepted: 9 November 2021

Published: 11 November 2021

Publisher's Note: MDPI stays neutral with regard to jurisdictional claims in published maps and institutional affiliations.

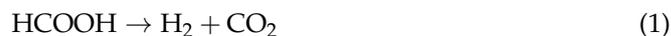


Copyright: © 2021 by the authors. Licensee MDPI, Basel, Switzerland. This article is an open access article distributed under the terms and conditions of the Creative Commons Attribution (CC BY) license (<https://creativecommons.org/licenses/by/4.0/>).

1. Introduction

With the rapid development of social science and technology, a large amount of traditional fossil energy is consumed in the process of industrialization. The consumption of fossil energy has produced a series of problems such as energy crisis and environmental pollution, which makes human society put forward an urgent demand for a new energy system [1,2]. Hydrogen, with the major advantages of cleanness, high efficiency, high energy density (142 MJ·kg⁻¹) and renewability, is one of the most promising energy carriers [3]. However, the preparation, storage, transportation and conversion of hydrogen are the main obstacles to the practical application of hydrogen [4,5]. At present, liquid phase hydrogen storage materials, which store hydrogen energy in the form of chemical bonds and produce hydrogen by catalytic dehydrogenation, are considered to be safe and efficient candidate materials [6,7]. Among them, hydrogen mass density and volume capacity of formic acid (FA) are as high as 4.4 wt% and 53.4 g·L⁻¹, respectively. It is a non-toxic, harmless and cheap chemical hydrogen storage material that can effectively avoid the problem of hydrogen storage and transportation [8,9]. Through a cycle constituted of dehydrogenation of FA and CO₂ hydrogenation, C1 resources can be effectively recycled, and zero carbon dioxide emission can be realized in theory, which is of great significance in the field of energy and environment [10,11]. Under appropriate catalyst and reaction conditions, FA can be decomposed either through dehydrogenation (Equation (1)) or dehydration (Equation (2)). Obviously, the key to promote the practical application of

FA as hydrogen storage material is to design and synthesize highly active and selective catalysts to decompose FA to hydrogen through dehydrogenation reaction.



A large number of research results showed that almost all heterogeneous catalysts effective for the decomposition of FA to hydrogen contain metal Pd, yet their catalytic activity and selectivity still cannot meet the requirements of practical application [12,13]. By introducing another metal to form Pd-based alloy catalysts, such as Pd-Au and Pd-Ag, the adsorption force of Pd on FA could be adjusted to promote dehydrogenation efficiency [14]. In addition, metal nanoparticles with small particle size usually show superior catalytic performance than large nanoparticles in FA dehydrogenation. Typically, capping agents are used in the preparation of small metal particles to resist thermodynamic instability due to their high surface energy [15,16]. However, capping molecules will pollute the active sites and result in the loss of catalytic activity. Therefore, anchoring active metal nanoparticles on suitable supports is an effective strategy for producing stable small particles and ensuring optimal catalyst utilization [17–19]. Porous carbon materials are ideal supports on account of its large surface area, well-developed pore structure and acid and alkali resistant properties [20,21]. Masuda et al. reported that Pd nanoparticles supported commercial Maxsorb carbon MSC-30, which had a high turnover frequency value for Pd/MSC-30 of FA decomposition that reached 5638 h^{-1} at $75 \text{ }^\circ\text{C}$ [22]. Lee et al. prepared hierarchically porous graphene-like carbon (KIE-8) support by chitosan, urea and KOH mixture pyrolysis methods, and the resulting catalyst for FA decomposition was 287 h^{-1} at room temperature [23].

The natural biomass material is rich in carbon elements, renewable, easy to process and is low cost as a potential carbon material precursor [24–26]. However, the pore structure of carbon materials prepared by direct pyrolysis of biomass precursors is generally underdeveloped and mostly has block structures and single chemical compositions, so it is not suitable for use as support materials [27,28]. Therefore, the activation of biomass carbon materials is an auxiliary but essential strategy for improving the material's chemical state, internal 3D network and nanostructures [29]. Promoters such as sodium hydroxide/potassium (KOH/NaOH), potassium chloride (KCl), potassium carbonate (K_2CO_3), zinc chloride (ZnCl_2) and phosphoric acid (H_3PO_4) are usually mixed with biomass precursors to form porous structures. The basic mechanism is that the surface carbon of biomass can be consumed by activators at high temperature so as to introduce layered porosity [30]. Nuilek et al. reported that the specific surface area of biomass carbon could be improved by activating *Urtica* with KOH [31]. With H_3PO_4 activation of xylan, the specific surface area of carbons increased from 548 to $1558 \text{ m}^2 \cdot \text{g}^{-1}$ [32].

According to information compiled by China Rural Statistical Yearbook, the total peanut and melon seed productions were estimated at about 17.52 million tons and 26.64 million tons in 2019 [33]. If the shell accounts for 30% of the total weight, about 6 million tons of peanut shell and 9 million tons of melon seed shell can be produced. As by-products, most of them are discarded or burned, except for a few that are used in processing animal feed and edible fungus culture medium, resulting in a serious waste of resources and environmental pollution [34,35]. Using them as precursor of biomass carbon is a win-win strategy, which not only can realize resource utilization of agricultural waste but also achieve the goals of carbon neutrality and peak carbon dioxide emissions. Herein, a series of biomass carbon supports was prepared by pyrolysis of peanut shell and melon seed shell to synthesize Pd/C catalyzed dehydrogenation of FA. The influence of the support structure and surface properties on the catalytic performance of the catalyst was discussed. As a result, the melon seed shell activated by ZnCl_2 was used as the best support, and it is supported Pd nanoparticles possessing high activity and stability for the decomposition of FA.

2. Materials and Methods

2.1. Materials

Peanut seeds and melon seeds (the supermarket in Guiyang, China), formic acid (FA, HCOOH, Aladdin, AR, 98 vol%, Shanghai, China), sodium formate (SF, HCOONa, Aladdin, AR, 99.5 wt%, Shanghai, China), sodium borohydride (NaBH₄, Acros, AR, 98 wt%, Shanghai, China), zinc chloride (ZnCl₂, Macklin, GR, 99.8 wt%, Shanghai, China), nitric acid (HNO₃, Chengdu Kelong, AR, 65–68 vol%, Chengdu, China), hydrochloric acid (HCl, Chengdu Kelong, AR, 36–38 vol%) and palladium chloride (PdCl₄, Guiyan Platinum Industry, AR, 59.5 wt%, Guiyang, China) were not further purified. Ordinary deionized water was used as the reaction solvent.

2.2. Preparation of Catalysts

The peanut seed shell and melon shell were dried in an oven at 150 °C for 3 h, and their water contents measured by moisture meter were 10.28% and 10.00%, respectively. The dried biomasses were crushed by a crusher and sieved through 20 mesh. The samples were treated with a 50.0 vol% aqueous HNO₃ solution for 30 min and then washed with deionized water to neutral drying for standby. The treated biomasses were dispersed in a ZnCl₂ solution (the mass ratio of ZnCl₂ to biomass was 2) and stirred at room temperature for 24 h. After drying, the moisture contents of peanut seed shell and melon shell treated with ZnCl₂ were 9.72% and 9.57%, respectively. Biomass carbon was obtained by slow pyrolysis of biomass in a tubular furnace oven under continuous 200.0 mL·min⁻¹ N₂ flow at 800 °C (heating rate of 5 °C·min⁻¹) for 2 h. The obtained black carbonized samples were washed to neutral with a 0.5 vol% aqueous HCl solution and labeled as C_{PS}-ZnCl₂ and C_{MS}-ZnCl₂ after drying. The acquisition of C_{PS} and C_{MS} followed the above steps except ZnCl₂ activation.

H₂PdCl₄ was dropped into the support dispersed with deionized water by an incipient wetness method at 30 °C and stood for 24 h. Finally, the solids were reduced at a 0.1 mol·L⁻¹ NaBH₄ solution and dried at 80 °C vacuum oven for 2 h, and the reduced catalysts were marked as Pd/C_{PS} and Pd/C_{MS} and Pd/C_{PS}-ZnCl₂ and Pd/C_{MS}-ZnCl₂, in which the loads of Pd were 5 wt%.

2.3. Test of Catalysts

The decomposition of FA reaction was conducted in a three-necked flask (Figure S1). One neck of the reaction flask was reserved for introducing 10.0 mL of mixed solution of 1.0 mol·L⁻¹ FA and 1.0 mol·L⁻¹ SF, and another was connected to a gas burette. The third one was inserted into a thermocouple to measure the reaction temperature. After the mixed solution was injected to the reactor containing catalyst (n_{Pd}/n_{FA} = 0.2%), the volume of the produced gas was recorded by recording the displacement of water in the gas burette. Unless otherwise specified, the reaction was carried out at 30 °C.

The used catalyst was recovered from the reaction mixture by filtration and then continuously washed with deionized water. After drying, an FA/SF solution was added for the recycling experiment.

2.4. Calculation Method

The activity of catalysts was compared and discussed in terms of turnover number and (TON) calculated according Equation (3).

$$\text{TON} = \frac{PV}{2n_{\text{Pd}}RT} \quad (3)$$

P denotes atmospheric pressure (101325 Pa), V denotes the generated volume of gas, n_{Pd} denotes the total mole number of Pd atoms in the catalyst, R denotes the universal gas constant (8.3145 m³·Pa·mol⁻¹·K⁻¹) and T denotes 25 °C (298 K). TON_X denotes TON at X min.

2.5. Characterization of Catalysts

The moisture content of biomass was obtained by a moisture meter (SFY-20W, Shenzhen, China). Biomasses were detected using a NETZSCH thermogravimetry (TG) 209 instrument (Billerica, MA, USA) with a ramp rate of $5\text{ }^{\circ}\text{C}\cdot\text{min}^{-1}$. X-ray diffraction (XRD) analysis was recorded on a Bruker D8 diffractometer (Billerica, MA, USA, 40 kV and 30 mA) using Cu irradiation ($\lambda = 1.54178\text{ \AA}$). The structural characterization of the catalysts was measured by transmission electron microscopy (TEM) using a Phillips Analytical FEI Talos-S (Tokyo, Japan) operated at 200 kV. The surface area and pore volume were performed by means of N_2 adsorption/desorption at $-196\text{ }^{\circ}\text{C}$, after dehydration under vacuum at $180\text{ }^{\circ}\text{C}$ for 6 h using ASAP 2460 (Norcross, GA, USA). According to the Brunauer–Emmett–Teller (BET) model, Barrett–Joyner–Halenda (BJH) method and the t-plot method, the surface areas, mesoporous volume and microporous volume were estimated, respectively. Scanning electron microscopy (SEM, ZEISS SIGMA, Tokyo, Japan) was used to observe the surface morphology of the catalysts. The contact angles of the catalysts were determined by using a Drop Shape Analysis System (Kruss DSA-100, Hamburg, Germany). Fourier Transform infrared spectroscopy (FTIR, IRAffinity-15, Shimane, Japan) was applied to record the absorption spectra of the catalysts. X-ray photoelectron spectroscopy (XPS) was carried out on a Fisher K-Alpha (Waltham, MA, USA) with monochromatic Al $K\alpha$ (1486.7 eV) as an X-ray source. The metal content was determined by inductively coupled plasma optical emission spectroscopy (ICP-OES, Agilent ICPOES730, Santa Clara, California, U.S.). The reactive products generated from FA were determined by a GC-9560 (Shimane, Japan) with TCD detector (TDX-01 column) and hydrogen flame ionization detector (FID, Porapak-Q col-umn, Zurich, Switzerland).

3. Results and Discussion

3.1. Catalyst Characterization Results

TG analysis was used to explore the changes of biomasses during pyrolysis. As shown in Figure 1a, weight loss in the first stage occurred at about $110\text{ }^{\circ}\text{C}$, which was due to water evaporation, and about 10% of weight loss was also consistent with the water content in biomasses. The obvious weight loss in the second stage appeared at $200\text{--}500\text{ }^{\circ}\text{C}$, which might be caused by hemicellulose, cellulose and lignin decomposition [36,37]. When the temperature raised to $800\text{ }^{\circ}\text{C}$, weight loss of all samples tended to be stable, and weight loss rates were about 75%. The XRD pattern of the catalyst is shown in Figure 1b. These catalysts had a broad peak at about $2\theta = 24^{\circ}$ and 44° , corresponding to the (002) and (100) planes of carbon (PDF#01-0604). The diffraction peaks of Pd/ C_{PS} and Pd/ C_{MS} at 40.0° , 46.7° and 68.1° belonged to (111), (200) and (220) planes of Pd, respectively (PDF#01-1310). In Table 1, the average particle sizes of Pd/ C_{PS} and Pd/ C_{MS} calculated by the Scherrer equation (Equation (S1)) were 7.2 and 6.8 nm, while Pd/ $\text{C}_{\text{PS}}\text{-ZnCl}_2$ and Pd/ $\text{C}_{\text{MS}}\text{-ZnCl}_2$ with smaller particle sizes showed weak Pd diffraction peaks, which indicated that ZnCl_2 activated supports could prevent the aggregation of Pd particles.

The dispersion of Pd particles was further observed by TEM. As displayed in Figure 2, Pd/ C_{PS} and Pd/ C_{MS} had large particle sizes and wide distributions. Pd/ $\text{C}_{\text{PS}}\text{-ZnCl}_2$ and Pd/ $\text{C}_{\text{MS}}\text{-ZnCl}_2$ had uniformly dispersed nanoparticles with average particle sizes of 3.6 and 2.9 nm, which was consistent with the results obtained by XRD. Therefore, ZnCl_2 activation had a great influence on the particle size of Pd, which might be related to the structure and properties of the support.

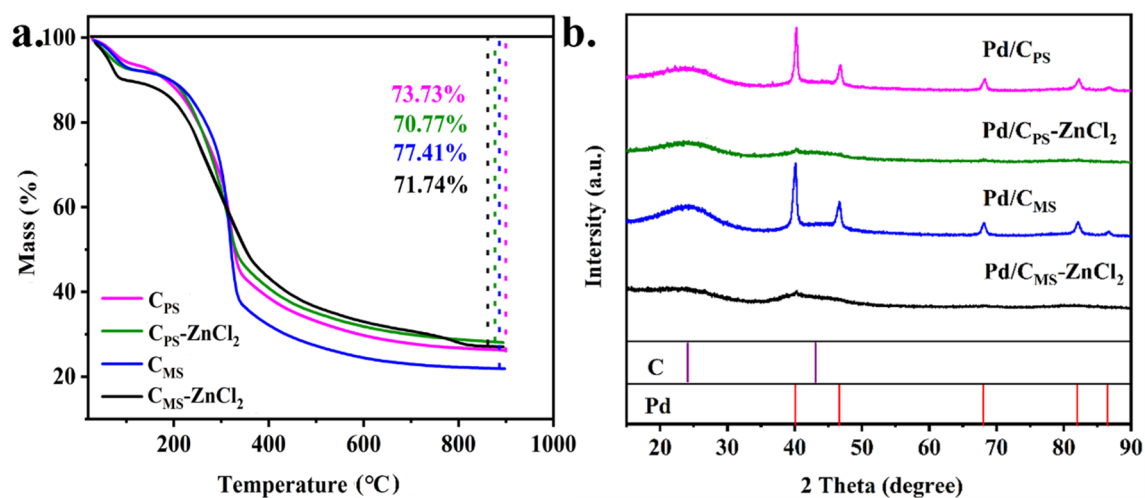


Figure 1. (a) TG curves of various supports and (b) XRD pattern of various catalysts.

Table 1. Pd particle sizes of various catalysts.

Catalyst	Average Particle Size (nm)	
	XRD	TEM
Pd/C _{PS}	7.2	6.7 ± 0.6
Pd/C _{PS} -ZnCl ₂	3.8	3.6 ± 0.6
Pd/C _{MS}	6.8	6.4 ± 0.4
Pd/C _{MS} -ZnCl ₂	2.8	2.9 ± 0.5

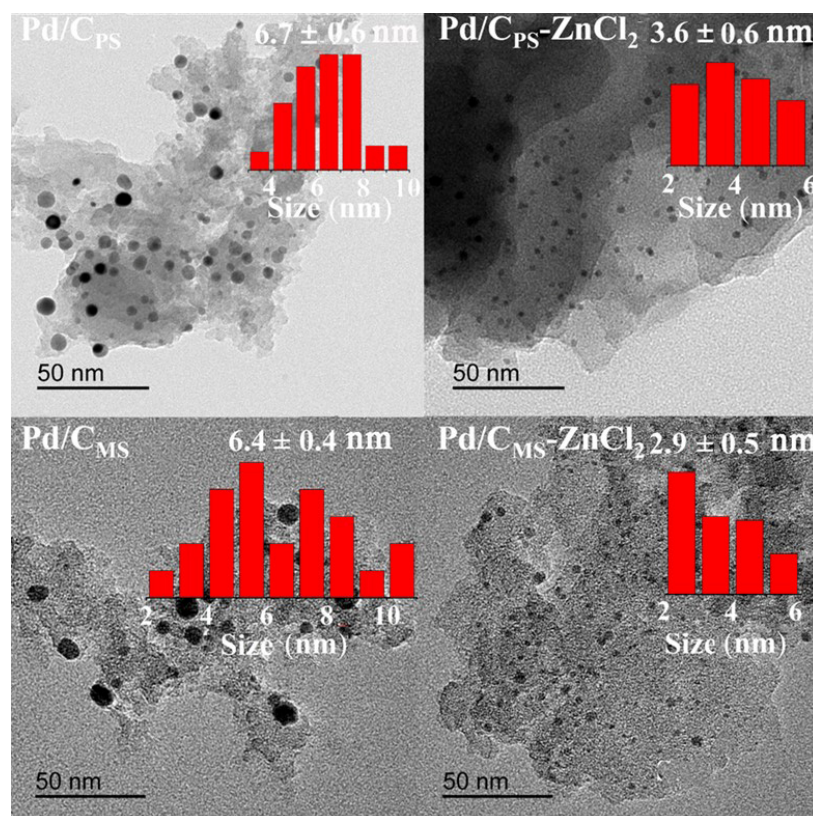


Figure 2. TEM micrographs and particle size distribution of various catalysts.

Figure 3a,b demonstrated the N_2 adsorption–desorption isotherms and the corresponding pore diameter distribution curves of the catalysts, and the corresponding calculation results are listed in Table 2. Type I isotherms in all catalysts confirmed microporous structure. Through the activation of $ZnCl_2$, the specific surface area of $Pd/C_{PS}-ZnCl_2$ increased from 456 to $629\text{ m}^2\cdot\text{g}^{-1}$. Moreover, the surface area of $Pd/C_{MS}-ZnCl_2$ was $1081\text{ m}^2\cdot\text{g}^{-1}$, which was about 3-fold larger than that of Pd/C_{MS} ($466\text{ m}^2\cdot\text{g}^{-1}$). It is rational that $ZnCl_2$ reacted with O_2 to form ZnO and Cl_2 , and the produced ZnO can further react with C atoms to generate CO_2 and Cl_2 in order to achieve the purpose of pore making [25,38]. When P/P_0 was close to one, the adsorption capacity of all catalysts tended to be saturated and had no obvious hysteresis loop, which indicated that they had relatively small micropores. It can be observed from Figure 3b that the pore size of the catalysts was mainly distributed between 0.34 and 0.55 nm. Whether melon seed shells or peanut shells were used as precursor, the microporous structure of the catalysts activated by $ZnCl_2$ was more abundant. Moreover, the micropore volume of $Pd/C_{MS}-ZnCl_2$ increased significantly from 0.20 to $0.44\text{ cm}^3\cdot\text{g}^{-1}$, which might depend on the nature of the biomass itself. The morphologies of $Pd/C_{PS}-ZnCl_2$ and $Pd/C_{MS}-ZnCl_2$ were characterized by SEM. In contrast to the disordered porous carbon obtained by carbonization of peanut seed shell (Figure 3c), the structure of melon shell presented a uniform cylindrical honeycomb (Figure 3d).

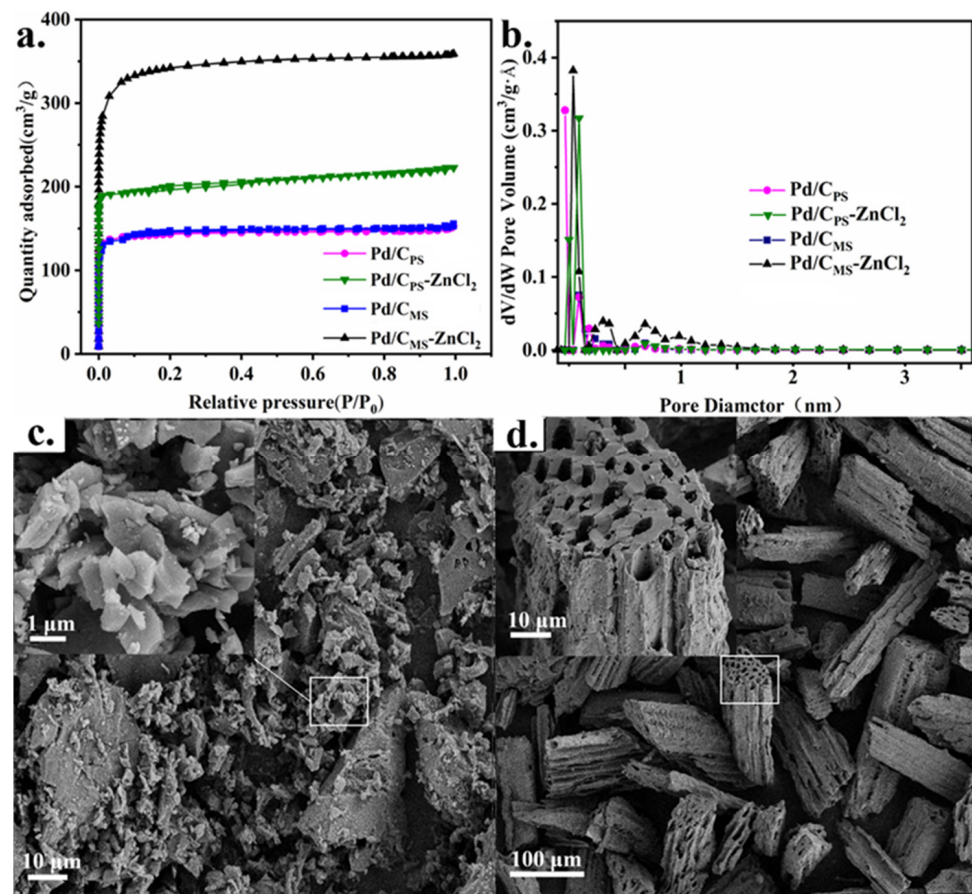


Figure 3. (a) N_2 absorption–desorption isotherms and (b) pore sizes distribution of various catalysts. (c) SEM images of $Pd/C_{PS}-ZnCl_2$ and (d) $Pd/C_{MS}-ZnCl_2$.

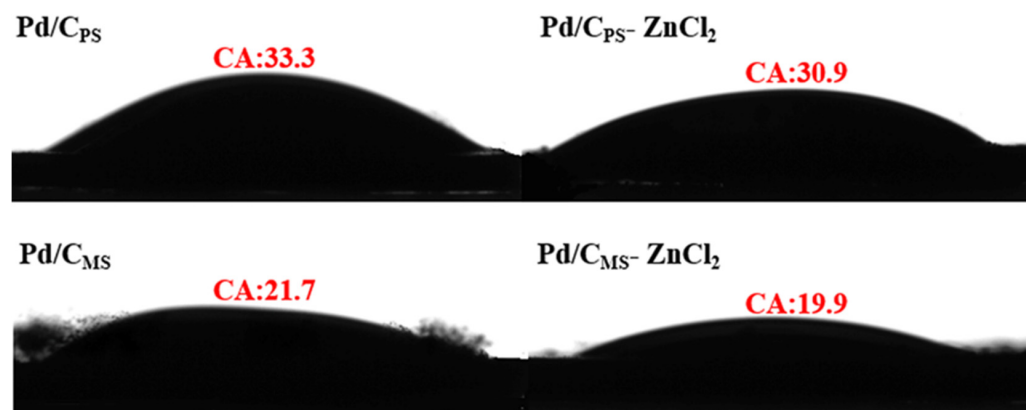
Table 2. Textural properties of various catalysts.

Catalyst	SSA _{BET} ¹ (m ² ·g ⁻¹)	SSA _{Mes} ² (m ² ·g ⁻¹)	SSA _{Mic} ³ (m ² ·g ⁻¹)	V _T ⁴ (cm ³ ·g ⁻¹)	V _{Mes} ⁵ (cm ³ ·g ⁻¹)	V _{Mic} ⁶ (cm ³ ·g ⁻¹)
Pd/C _{PS}	456	50	406	0.23	0.03	0.20
Pd/C _{PS} -ZnCl ₂	629	113	517	0.34	0.09	0.25
Pd/C _{MS}	466	50	416	0.24	0.04	0.20
Pd/C _{MS} -ZnCl ₂	1081	199	882	0.55	0.11	0.44

¹ Specific surface area, ² mesopore and ³ micropore specific surface area. ⁴ Total pore volume, ⁵ mesopore and ⁶ micropore pore volume.

In addition to the structure and morphology analyzed in the previous discussion, the surface properties of catalysts are also keys for determining its catalytic performance. The isoelectric point (IEP) test showed that Pd/C_{PS} and Pd/C_{MS} had similar isoelectric points, which were 5.4 and 5.5 respectively. After activation, the isoelectric points of Pd/C_{PS}-ZnCl₂ and Pd/C_{MS}-ZnCl₂ increased to 6.5 and 6.9. From the reaction mechanism, FA is adsorbed on the Pd surface through deprotonation to form HCOO⁻. Therefore, high H⁺ concentration is harmful because too many H⁺ may promote the recombination of HCOO⁻ with H⁺ and/or delay the deprotonation step, resulting in the reduction in FA dehydrogenation rate [39].

It could be seen from the photographs of water droplets on the catalyst thin films in Figure 4 that the contact angles of Pd/C_{PS}, Pd/C_{PS}-ZnCl₂, Pd/C_{MS} and Pd/C_{MS}-ZnCl₂ were 33.3°, 30.9°, 21.7° and 19.9°, respectively. Pd/C_{MS}, Pd/C_{MS}-ZnCl₂ obtained by carbonization of melon seed shell had higher hydrophilicity. Solid catalysts with strong hydrophilicity can improve the interface and enhance the performance of heterogeneous catalysts [40]. FTIR spectra analysis exhibited that the catalysts had absorption peaks at 3427.1 and 3427.7 cm⁻¹ corresponding to the presence of an O-H group, and the peak at 1119.2 and 1123.3 cm⁻¹ could be ascribed to a C-OH group (Figure S2). Due to the breaking and recombination of chemical bonds during biomass pyrolysis, a large number of oxygen-containing functional groups were formed on the surface of biomass carbon, which was also the main feature of biomass carbon that was different from other carbons [41].

**Figure 4.** Photographs of water droplets on various catalysts thin film together with their contact angles.

XPS spectra were used to analyze surface composition and chemical state of the catalysts. Figure 5a presented that the O 1s XPS spectra could be divided into four types of oxygen-containing functional groups: O1 (quinones, 530.8–531.3 eV), O2 (ethers or phenolic hydroxyl, 532.4–532.8 eV), O3 (lactone or carboxyl, 533.4–534.0 eV) and O4 (adsorbed O₂ or H₂O, 535.0–535.8 eV) [42], and the corresponding atomic ratios were listed in Table S1. The surface O content of Pd/C_{PS}-ZnCl₂ and Pd/C_{MS}-ZnCl₂ increased by 63% and 55%, respectively, after ZnCl₂ activation. Previous studies have showed that the oxygen-containing functional group on the surface of the support can be used as the nucleation point of metal particles to promote the interaction between the support and metal particles so as to form smaller nanoparticles [43,44]. Compared with Pd/C_{MS} (7.33 at%), activated

Pd/C_{MS}-ZnCl₂ had more O₂ and O₃ contents (11.71 at%). At the same time, similar results were observed in the other group. The increase in O₂ and O₃ might increase the hydrophilicity of the catalyst to a certain extent [45]. From C 1s spectra (Figure 5b), the content of aromatic C (284.8 eV) [46] in all samples accounts for about 70%–80% of the total C content (Table S2). It was found that ZnCl₂ activation reduced the content of aromatic C. In addition, phenolic C (286.4 eV) and aliphatic and carboxylic C (287.8 eV) were observed on the surface of catalysts. The ashes were obtained by calcining the sample at 650 °C for 2 h. The results revealed that the carbonization of peanut shell produced more ash than melon seed shell, and the ash content would decrease with the introduction of ZnCl₂. In the XPS spectra of Pd 3d 5/2 (Figure 5c), two peaks were fitted well at 335.8 and 337.8 eV, relating to Pd⁰ and Pd²⁺, respectively. As observed in Table S3, there was no significant difference in the electronic state of Pd between different catalysts. Moreover, the Pd content of all catalysts was similar, both from the surface content determined by XPS and the bulk content determined by ICP.

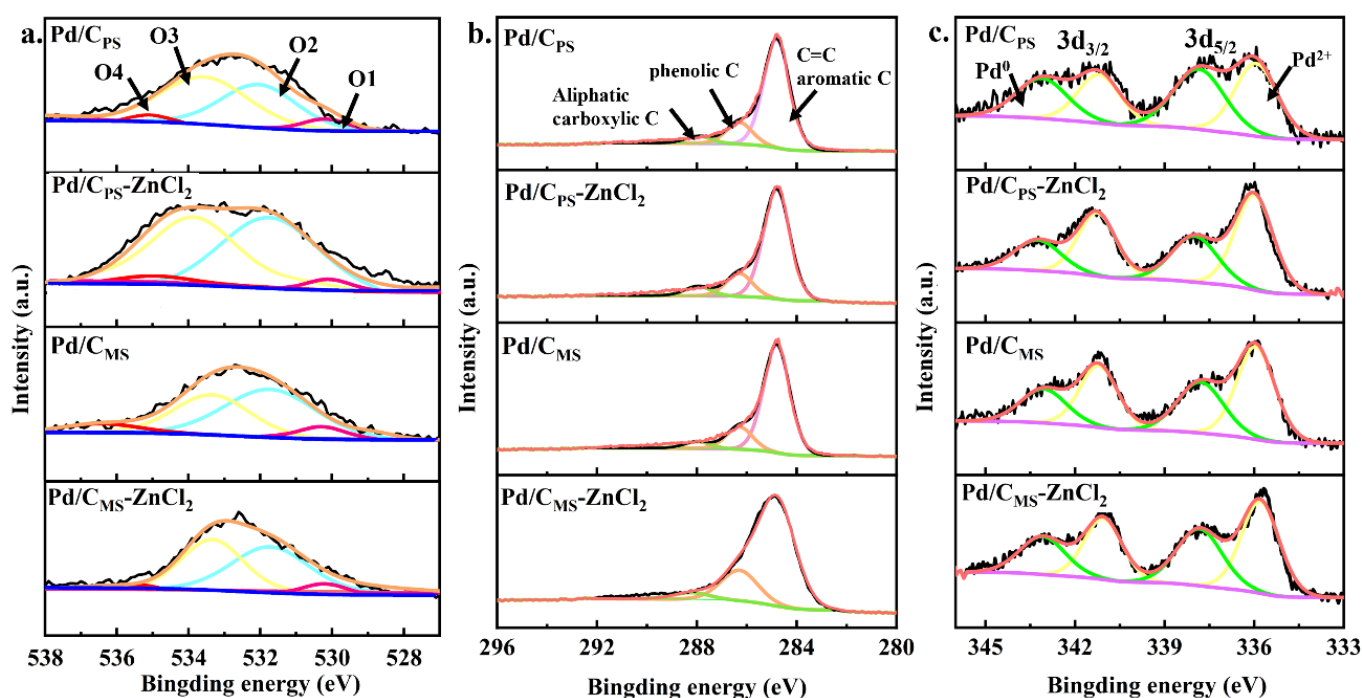


Figure 5. XPS patterns of (a) O 1s, (b) C 1s and (c) Pd 3d of various catalysts.

3.2. Catalytic Activity

The performance of the catalyst with different biomass supports the total volume ($H_2 + CO_2$) production at 30 °C as presented in Figure 6a. The best catalytic activity was observed for Pd/C_{MS}-ZnCl₂ in which the reaction was completed in 120 min, providing TON₁₂₀ with a value of 484.3 (Table S4). The generated gas was determined by GC to be H₂ and CO₂ with the molar ratio of 1:1, where CO was below the detection limit (<1 ppm) (Figures S3 and S4). Similarly, Pd/C_{PS}-ZnCl₂ showed the second-best catalytic performance, with a TON₁₂₀ value of 462.5 and conversion of 95% at 120 min. However, under the same conditions, the TON₁₂₀ values of Pd/C_{MS} and Pd/C_{PS} were only 168.5 and 130.6, and the corresponding conversion rates were 34% and 27%, respectively. The relationship between specific catalytic activity expressed in TON and Pd particle size is observed in Figure 6b. The size of Pd particles was negatively correlated with the TON value of the catalysts, mainly because the Pd with smaller particle size had more active sites [47,48]. Moreover, the smaller nanoparticles had a “clean” surface (uncapped) and more active edge/corner atoms, so they showed excellent catalytic performance [13,49].

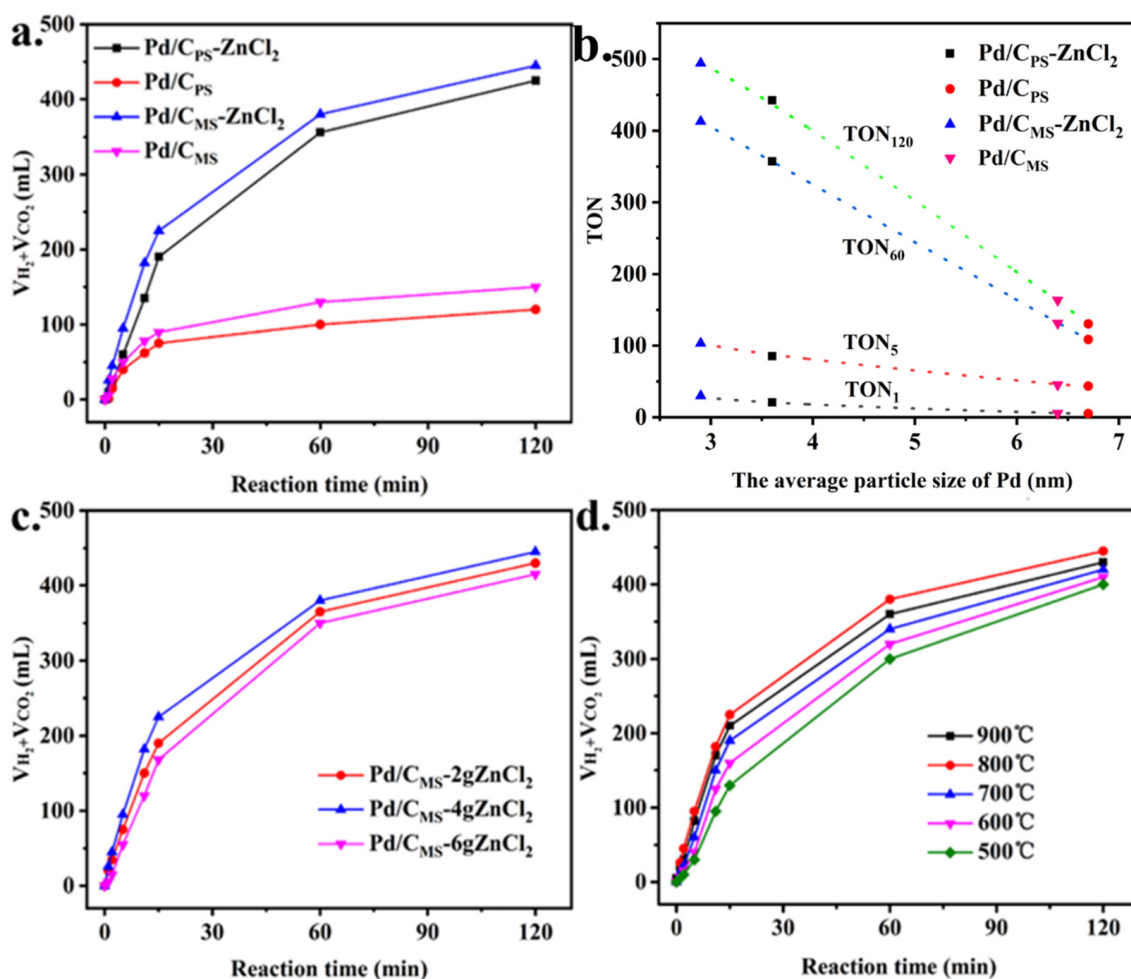


Figure 6. Total volume ($H_2 + CO_2$) generation catalyzed by (a) various catalysts, (c) Pd/C_{MS} with different ZnCl₂ masses activated and (d) Pd/C_{MS}-ZnCl₂ with different carbonization temperature from FA. (b) Various catalysts with corresponding TON value vs. particle size of various catalysts.

Through the characterization and performance evaluation of the catalysts, the supports played an important role in the activity of the catalysts. During the preparation of the supports, ZnCl₂ had the functions of swelling, catalytic dehydration and pore forming in the treatment of biomass raw materials [50]. Therefore, the action of ZnCl₂ activating biomass to obtain biomass carbon support with large specific surface areas was of great significance in reducing metal particles size and improving dispersion, as it increased catalyst activity. In addition, more oxygen-containing functional groups could be obtained through ZnCl₂ activation, which could boost the dispersion of Pd nanoparticles and reduced surface acidity for the purpose of improving catalytic performance. Another important factor affecting the structure and surface properties of the supports depends on the properties of the raw material. Compared with peanut shells, the catalyst prepared by carbonizing melon seed shell had larger specific surface areas, higher hydrophilicity and uniform honeycomb morphology. Therefore, the selection of appropriate biomass precursors was also key to the preparation of high-performance catalysts.

The activity of catalysts prepared by activation of ZnCl₂ with different masses on the decomposition of FA is observed in Figure 6c. The TON₁ values of Pd/C_{MS}-2gZnCl₂ and Pd/C_{MS}-6gZnCl₂ catalyzed FA decomposition were 12.8 and 5.4. By comparison, the TON₁ value of Pd/C_{MS}-4gZnCl₂ was 2-fold and 5-fold higher than those of Pd/C_{MS}-2gZnCl₂ and Pd/C_{MS}-6gZnCl₂, respectively. Therefore, it could be inferred that the quality of ZnCl₂ affects activation efficiency. A suitable amount of ZnCl₂ could adjust the porous structure of biomass carbons; in contrast, excessive ZnCl₂ was likely to boost the volatilization of

surface species of the support so as to widen the pores and reduce the surface area of biomass carbons [51].

Biomass carbon was mainly composed of aromatic carbon, amorphous carbon and ash, and the content of each part was mainly determined by pyrolysis temperature [52]. The swelling function of ZnCl_2 and the release of small molecular gases could catalyze the aromatization reaction at temperature ≥ 400 °C and generate a large number of pore structures [36]. Therefore, the effect of carbonization temperature on catalyst activity was investigated from 500 °C (Figure 6d). When the carbonization temperature was 500 °C, the TON_1 value of the catalyst was only 4.4. With the increase in carbonization temperature, the catalytic activity of the prepared catalyst gradually increased, and the TON_1 value of 28.3 was the largest at 800 °C. This might be because at lower temperatures, water, CO and CO_2 in biomass volatilize to form amorphous carbon. With the increase in temperature, alkyl carbon and oxyalkyl carbon fractured in biomass and gradually rearranged into aryl carbon [53,54]. Among them, aromatic hydrocarbon carbon has strong stability, and this structure of biomass carbon was also an important reason for its stability. However, the TON_1 value of Pd/ C_{MS} -900 was 14.1. From the previous discussion, it could be seen that the surface oxygen-containing functional groups could promote the activity of the catalyst, while O content decreased with the increase in temperature, which might be the reason for decreased catalytic activity with the continuous increase in carbonization temperature.

The activity of Pd/ C_{MS} - ZnCl_2 for FA decomposition at 20–60 °C was investigated in Figure 7a. With the increase in reaction temperature, the gas generation rate increased obviously, providing the TON_1 values of 15.0, 28.3, 42.5, 63.1 and 100.1. The stability of the catalyst was important for practical applications. After three cycles, catalytic activity decreased to a certain extent (Figure 7b). TEM characterization of the catalyst after the reusability test found that the average particle size increased from the initial 2.9 nm (Figure 2) to 3.2 nm (Figure 7c). XPS characterization of the catalyst after the reaction demonstrated that the content of Pd^0 decreased (Figure S5). In the dehydrogenation of formic acid, Pd^0 is conducive to the activation of C-H bond, which is often the rate controlling step of dehydrogenation [50,55,56]. Therefore, the decrease in catalyst Pd^0 in the process might also be another reason for the decline of activity.

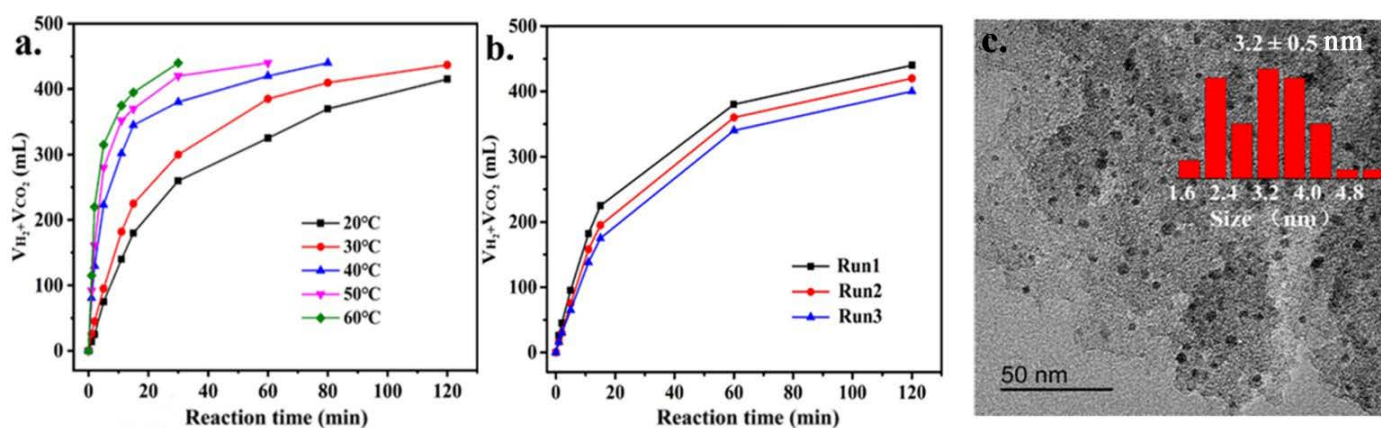


Figure 7. (a) Total volume ($\text{H}_2 + \text{CO}_2$) generation catalyzed by Pd/ C_{MS} - ZnCl_2 at different reaction temperatures and (b) stability test for the decomposition for FA. (c) TEM micrographs and particle size distribution of the recycled Pd/ C_{MS} - ZnCl_2 .

4. Conclusions

To sum up, high efficiency Pd nanoparticles were loaded on peanut shell and melon seed shell derived porous carbon for FA dehydrogenation. The catalysts obtained from biomass activated by ZnCl_2 had Pd particle size distributions of 2.9 nm (Pd/ C_{MS} - ZnCl_2) and 3.6 nm (Pd/ C_{PS} - ZnCl_2), which were smaller than those of the unactivated catalyst. The analysis showed that the specific surface area of the catalysts was improved by ZnCl_2 treatment; Pd/ C_{MS} - ZnCl_2 , in particular, had a high specific surface area of $1081 \text{ m}^2 \cdot \text{g}^{-1}$.

In addition, ZnCl₂ also affected the surface properties of catalysts. The surface O content of Pd/C_{PS}-ZnCl₂ and Pd/C_{MS}-ZnCl₂ increased by 63% and 55%, respectively. Moreover, the activated catalysts were closer to neutral, which would be conducive to the removal of H⁺ from FA. The properties of biomass also determined the performance of the catalyst. Notably, Pd/C_{MS}-ZnCl₂ afforded the highest TON₁ value, reaching up to 28.3 at 30 °C, which is higher than that of Pd/C_{PS}-ZnCl₂ (19.0). The Pd/C_{MS}-ZnCl₂ with melon seed shells as precursor had higher specific surface area; thus, it could provide more sites for Pd nanoparticles. Moreover, its homogeneous honeycomb structure and stronger hydrophilicity further promoted the decomposition rate of liquid FA. This study not only provides a method for using agricultural waste as a carbon source of porous carbon but also accelerates FA as a high-efficiency hydrogen supplier in mobile devices.

Supplementary Materials: The following are available online at <https://www.mdpi.com/article/10.3390/nano11113028/s1>, Figure S1: Experimental apparatus of H₂ generation from the FA dehydrogenation, Equation (S1): The average particles sizes were estimated from XRD by Debye-Scherrer, Figure S2: The spectrum of various catalysts, Figure S3: GC spectrum using TCD for the gas from FA over Pd/C_{MS}-ZnCl₂, Figure S4: GC spectrum using PDHID for the standard gas and the gas from FA over Pd/C_{MS}-ZnCl₂, Figure S5: XPS patterns of Pd 3d of Pd/C_{MS}-ZnCl₂ before and after reaction, Table S1: O content of various catalysts (at.%), Table S2: C content and Ash of various catalysts, Table S3: Pd content of various catalysts, Table S4: FA dehydrogenation catalyzed by various catalysts.

Author Contributions: Writing—original draft preparation, T.C.; data curation, J.C.; software, supervision, J.M.; methodology, C.Y.; writing—original draft and editing, M.Y.; supervision, F.L.; software, M.D.; resources, X.W.; funding acquisition, Y.R. All authors have read and agreed to the published version of the manuscript.

Funding: This research was funded by Innovation Group Project of Education Department in Guizhou Province (NO. 2021010), One Hundred Person Project of Guizhou Province (NO. 20165655), the Ph.D Foundation of Guizhou University (NO. X2021017), the cultivation project of Guizhou University (NO. [2020]38), Natural Science Special Foundation of Guizhou University (NO. X2021073 Special Post D), Excellent Young Scientific and Technological Talent Program of Guizhou Province (NO. 20195645) and Zunyi City Innovative Talent Team Project (NO. 20195645).

Data Availability Statement: Not applicable.

Acknowledgments: The authors thank the contributions of Jinke Cheng, Jun Ma, Chunliang Yang, Mengqin Yao, Fei Liu, Min Deng, Xiaodan Wang and Yuan Ren, including purchasing materials and conducting relative experiments.

Conflicts of Interest: The authors declare no conflict of interest.

References

1. Gao, Y.; Xue, Y.; Liu, T.; Liu, Y.; Zhang, C.; Xing, C.; He, F.; Li, Y. Bimetallic mixed clusters highly loaded on porous 2D graphdiyne for hydrogen energy conversion. *Adv. Sci.* **2021**, *8*, 2102777. [[CrossRef](#)]
2. Yue, M.; Lambert, H.; Pahon, E.; Roche, R.; Jemei, S.; Hissel, D. Hydrogen energy systems: A critical review of technologies, applications, trends and challenges. *Renew. Sustain. Energy Rev.* **2021**, *146*, 111180. [[CrossRef](#)]
3. Olabi, A.G.; Bahri, A.; Abdelghafar, A.A.; Baroutaji, A.; Sayed, E.T.; Alami, A.H.; Rezk, H.; Abdelkareem, M.A. Large-vs-scale hydrogen production and storage technologies: Current status and future directions. *Int. J. Endocrinol.* **2021**, *46*, 23498–23528. [[CrossRef](#)]
4. Hirscher, M.; Yartys, V.A.; Baricco, M.; Bellosta, J.; Blanchard, D.; Bowman, R.C.; Broom, D.P.; Buckley, C.E.; Chang, F.; Chen, P.; et al. Materials for hydrogen-based energy storage e past, recent progress and future outlook. *J. Alloys Compd.* **2020**, *827*, 153548. [[CrossRef](#)]
5. Tarhan, C.; Cil, M.A. A study on hydrogen, the clean energy of the future: Hydrogen storage methods. *J. Energy Storage* **2021**, *40*, 102676. [[CrossRef](#)]
6. Aakko-Saksa, P.T.; Cook, C.; Kiviahio, J.; Repo, T. Liquid organic hydrogen carriers for transportation and storing of renewable energy-review and discussion. *J. Power Sources* **2018**, *396*, 803–823. [[CrossRef](#)]
7. Zheng, J.; Zhou, H.; Wang, C.; Ye, E.; Xu, J.W.; Loh, X.J.; Li, Z. Current research progress and perspectives on liquid hydrogen rich molecules in sustainable hydrogen storage. *Energy Storage Mater.* **2021**, *35*, 695–722. [[CrossRef](#)]

8. Shen, F.; Smith, R.L., Jr.; Li, J.; Guo, H.; Zhang, X.; Qi, X. Critical assessment of reaction pathways for conversion of agricultural waste biomass into formic acid. *Green Chem.* **2021**, *23*, 1536–1561. [[CrossRef](#)]
9. Takagaki, A.; Obata, W.; Ishihara, T. Oxidative conversion of glucose to formic acid as a renewable hydrogen source using an abundant solid base catalyst. *Chemistryopen* **2021**, *10*, 954–959. [[CrossRef](#)] [[PubMed](#)]
10. Tsai, H.M.; Lien, W.H.; Liao, C.H.; Chen, Y.T.; Huang, S.C.; Chou, F.P.; Chang, C.Y.; Yu, J.S.K.; Kao, Y.T.; Wu, T.K. Efficient and reversible catalysis of formic acid-carbon dioxide cycle using carbamate-substituted ruthenium-dithiolate complexes. *ChemCatChem* **2021**, *13*, 4092–4098. [[CrossRef](#)]
11. Sun, Q.; Chen, B.; Wang, N.; He, Q.; Chang, A.; Yang, C.M.; Asakura, H.; Tanaka, T.; Hulsey, M.J.; Wang, C.H.; et al. Zeolite-encaged Pd-Mn nanocatalysts for CO₂ hydrogenation and formic acid dehydrogenation. *Angew. Chem. Int. Ed. Engl.* **2020**, *59*, 20183–20191. [[CrossRef](#)] [[PubMed](#)]
12. Singh, A.K.; Singh, S.; Kumar, A. Hydrogen energy future with formic acid: A renewable chemical hydrogen storage system. *Catal. Sci. Technol.* **2016**, *6*, 12–40. [[CrossRef](#)]
13. Li, Z.; Xu, Q. Metal-nanoparticle-catalyzed hydrogen generation from formic acid. *Acc. Chem. Res.* **2017**, *50*, 1449–1458. [[CrossRef](#)]
14. Li, S.; Zhou, Y.; Kang, X.; Liu, D.; Gu, L.; Zhang, Q.; Yan, J.M.; Jiang, Q. A simple and effective principle for a rational design of heterogeneous catalysts for dehydrogenation of formic acid. *Adv. Mater.* **2019**, *31*, 1806781. [[CrossRef](#)] [[PubMed](#)]
15. Gao, Y.; Hu, E.; Yin, G.; Huang, Z. Pd nanoparticles supported on CeO₂ nanospheres as efficient catalysts for dehydrogenation from additive-free formic acid at low temperature. *Fuel* **2021**, *302*, 121142. [[CrossRef](#)]
16. Li, W.J.; Wey, M.Y. Dual immobilization of Pd Cu nanoparticles on halloysite nanotubes by CTAB and PVP for automobile exhaust elimination. *Appl. Clay Sci.* **2021**, *215*, 106312. [[CrossRef](#)]
17. Protasova, L.N.; Rebrov, E.V.; Choy, K.L.; Pung, S.Y.; Engels, V.; Cabaj, M.; Wheatley, A.E.H.; Schouten, J.C. ZnO based nanowires grown by chemical vapour deposition for selective hydrogenation of acetylene alcohols. *Catal. Sci. Technol.* **2011**, *1*, 768–777. [[CrossRef](#)]
18. Mori, K.; Dojo, M.; Yamashita, H. Pd and Pd–Ag nanoparticles within a macroreticular basic resin: An efficient catalyst for hydrogen production from formic acid decomposition. *ACS Catal.* **2013**, *3*, 1114–1119. [[CrossRef](#)]
19. Tan, H.; Wang, J.; Yu, S.; Zhou, K. Support morphology-dependent catalytic activity of Pd/CeO₂ for formaldehyde oxidation. *Environ. Sci. Technol.* **2015**, *49*, 8675–8682. [[CrossRef](#)]
20. Jing, H.; Ji, L.; Wang, Z.; Guo, J.; Lu, S.; Sun, J.; Cai, L.; Wang, Y. Synthesis of ZnO nanoparticles loaded on biochar derived from spartina alterniflora with superior photocatalytic degradation performance. *Nanomaterials* **2021**, *11*, 2479. [[CrossRef](#)] [[PubMed](#)]
21. Bukhari, Q.U.A.; Silveri, F.; Della Pelle, F.; Scroccarello, A.; Zappi, D.; Cozzoni, E.; Compagnone, D. Water-phase exfoliated biochar nanofibers from eucalyptus scraps for electrodemodification and conductive film fabrication. *ACS Sustain. Chem. Eng.* **2021**, *9*, 13988–13998. [[CrossRef](#)]
22. Masuda, S.; Mori, K.; Futamura, Y.; Yamashita, H. PdAg nanoparticles supported on functionalized mesoporous carbon: Promotional effect of surface amine groups in reversible hydrogen delivery/storage mediated by formic acid/CO₂. *AACS Catal.* **2018**, *8*, 2277–2285. [[CrossRef](#)]
23. Lee, D.; Jin, M.; Oh, D.; Lee, S.; Park, J. Straightforward synthesis of hierarchically porous nitrogen-doped carbon via pyrolysis of chitosan/urea/KOH mixtures and its application as a support for formic acid dehydrogenation catalysts. *ACS Sustain. Chem. Eng.* **2017**, *5*, 9935–9944. [[CrossRef](#)]
24. Du, W.; Zhang, Z.; Du, L.; Fan, X.; Shen, Z.; Ren, X.; Zhao, Y.; Wei, C.; Wei, S. Designing synthesis of porous biomass carbon from wheat straw and the functionalizing application in flexible, all-solid-state supercapacitors. *J. Alloys Compd.* **2019**, *797*, 1031–1040. [[CrossRef](#)]
25. Wang, Y.; Qu, Q.; Gao, S.; Tang, G.; Liu, K.; He, S.; Huang, C. Biomass derived carbon as binder-free electrode materials for supercapacitors. *Carbon* **2019**, *155*, 706–726. [[CrossRef](#)]
26. Dubey, P.; Shrivastav, V.; Maheshwari, P.H.; Sundriyal, S. Recent advances in biomass derived activated carbon electrodes for hybrid electrochemical capacitor applications: Challenges and opportunities. *Carbon* **2020**, *170*, 1–29. [[CrossRef](#)]
27. Qiu, C.; Chen, Q.; Chang, C.; Jiang, W.; Fan, G. Mechanochemically assisted fabrication of ultrafine Pd nanoparticles on natural waste-derived nitrogen-doped porous carbon for the efficient formic acid decomposition. *Int. J. Endocrinol.* **2021**, *46*, 656–665. [[CrossRef](#)]
28. El-Azazy, M.; Nabil, I.; Hassan, S.S.; El-Shafie, A.S. Adsorption characteristics of pristine and magnetic olive stones biochar with respect to clofazimine. *Nanomaterials* **2021**, *11*, 963. [[CrossRef](#)]
29. Xu, C.; Stromme, M. Sustainable porous carbon materials derived from wood-based biopolymers for CO₂ capture. *Nanomaterials* **2019**, *9*, 103. [[CrossRef](#)]
30. Ismail, I.S.; Singh, G.; Smith, P.; Kim, S.; Yang, J.; Joseph, S.; Yusup, S.; Singh, M.; Bansal, V.; Talapaneni, S.N.; et al. Oxygen functionalized porous activated biocarbons with high surface area derived from grape marc for enhanced capture of CO₂ at elevated-pressure. *Carbon* **2020**, *160*, 113–124. [[CrossRef](#)]
31. Nuilek, K.; Wongwiriyapan, W.; Sattayarut, V.; Simon, A.; Koncz-Horvath, D.; Ferenczi, T.; Kristaly, F.; Baumli, P. Comparison of acid exfoliators in carbon nanosheets synthesis from stinging nettle (*urtica dioica*) for electrochemical applications. *Sci. Rep.* **2020**, *10*, 17270. [[CrossRef](#)]

32. Yi, Y.; Wu, S.; Luo, H.; He, L.; Yang, Y.; Xue, T.; Xu, J.; Wen, Y.; Wang, P. Soft template assisted hydrothermal synthesis of phosphorus doped porous carbon spheres with tunable microstructure as electrochemical nanozyme sensor for distinguishable detection of two flavonoids coupled with derivative voltammetry. *J. Electroanal. Chem.* **2021**, *897*, 115563. [CrossRef]
33. China Statistical Yearbook. Available online: <http://www.stats.gov.cn/tjsj/ndsj/2020/indexch.htm> (accessed on 2 November 2021).
34. Kempasiddaiah, M.; Sree Raj, K.A.; Kandathil, V.; Dateer, R.B.; Sasidhar, B.S.; Yelamaggad, C.V.; Sekhar Rout, C.; Patil, S.A. Waste biomass-derived carbon-supported palladium-based catalyst for cross-coupling reactions and energy storage applications. *Appl. Surf. Sci.* **2021**, *570*, 151156. [CrossRef]
35. Afolalu, S.A.; Salawu, E.Y.; Ogedengbe, T.S.; Joseph, O.O.; Okwilagwe, O.; Emetere, M.E.; Yusuf, O.O.; Noiki, A.A.; Akinlabi, S.A. Bioagro waste valorization and its sustainability in the industry: A review. *IOP Conf. Ser. Mater. Sci. Eng.* **2021**, *1107*, 012140. [CrossRef]
36. Lin, F.; Liu, X.; Ma, M.; Qi, F.; Pan, Y.; Wang, L.; Ma, P.; Zhang, Y. Real-time monitoring the carbonization and activation process of activated carbon prepared from Chinese parasol via zinc chloride activation. *J. Anal. Appl. Pyrol.* **2021**, *155*, 105089. [CrossRef]
37. Ozdemir, I.; Şahin, M.; Orhan, R.; Erdem, M. Preparation and characterization of activated carbon from grape stalk by zinc chloride activation. *Fuel Process. Technol.* **2014**, *125*, 200–206. [CrossRef]
38. Sun, L.; Tian, C.; Li, M.; Meng, X.; Wang, L.; Wang, R.; Yin, J.; Fu, H. From coconut shell to porous graphene-like nanosheets for high-power supercapacitors. *J. Mater. Chem. A* **2013**, *1*, 6462–6470. [CrossRef]
39. Jae, J.; Tompsett, G.A.; Foster, A.J.; Hammond, K.D.; Auerbach, S.M.; Lobo, R.F.; Huber, G.W. Investigation into the shape selectivity of zeolite catalysts for biomass conversion. *J. Catal.* **2011**, *279*, 257–268. [CrossRef]
40. Xing, C.; Zhang, Y.; Gao, Y.; Kang, Y.; Zhang, S. N, P co-doped microporous carbon as a metal-free catalyst for the selective oxidation of alcohols by air in water. *New J. Chem.* **2021**, *45*, 13877–13884. [CrossRef]
41. Cao, X.; Harris, W. Properties of dairy-manure-derived biochar pertinent to its potential use in remediation. *Bioresour. Technol.* **2010**, *101*, 5222–5228. [CrossRef] [PubMed]
42. Biniak, S.; Szymański, G.; Siedlewski, J.; Świątkowski, A. The characterization of activated carbons with oxygen and nitrogen surface groups. *Carbon* **1997**, *35*, 1799–1810. [CrossRef]
43. Pei, X.; Jiao, H.; Fu, H.; Yin, X.; Luo, D.; Long, S.; Gong, W.; Zhang, L. Facile construction of a highly dispersed Pt nanocatalyst anchored on biomass-derived N/O-doped carbon nanofibrous microspheres and its catalytic hydrogenation. *ACS Appl. Mater. Interfaces* **2020**, *12*, 51459–51467. [CrossRef]
44. Jin, M.; Park, J.; Oh, D.; Lee, S.; Park, J.; Lee, K.; Lee, D. Pd/NH₂-KIE-6 catalysts with exceptional catalytic activity for additive-free formic acid dehydrogenation at room temperature: Controlling Pd nanoparticle size by stirring time and types of Pd precursors. *Int. J. Endocrinol.* **2018**, *43*, 1451–1458. [CrossRef]
45. Li, J.; Liu, X.; Che, H.; Liu, C.; Li, C. Facile construction of O-doped crystalline/non-crystalline g-C₃N₄ embedded nano-homojunction for efficiently photocatalytic H₂ evolution. *Carbon* **2021**, *172*, 602–612. [CrossRef]
46. Song, F.; Wang, X.; Li, T.; Zhang, J.; Bai, Y.; Xing, B.; Giesy, J.P.; Wu, F. Spectroscopic analyses combined with gaussian and coats-redfern models to investigate the characteristics and pyrolysis kinetics of sugarcane residue-derived biochars. *J. Clean. Prod.* **2019**, *237*, 117855. [CrossRef]
47. Nishio, H.; Miura, H.; Kamata, K.; Shishido, T. Deposition of highly dispersed gold nanoparticles onto metal phosphates by deposition–precipitation with aqueous ammonia. *Catal. Sci. Technol.* **2021**. [CrossRef]
48. Wang, Z.; Liang, S.; Meng, X.; Mao, S.; Lian, X.; Wang, Y. Ultrasmall PdAu alloy nanoparticles anchored on amine-functionalized hierarchically porous carbon as additive-free catalysts for highly efficient dehydrogenation of formic acid. *Appl. Catal. B Environ.* **2021**, *291*, 120140. [CrossRef]
49. Wang, C.; Astruc, D. Recent developments of nanocatalyzed liquid-phase hydrogen generation. *Chem. Soc. Rev.* **2021**, *50*, 3437–3484. [CrossRef] [PubMed]
50. Li, J.; Chen, W.; Zhao, H.; Zheng, X.; Wu, L.; Pan, H.; Zhu, J.; Chen, Y.; Lu, J. Size-dependent catalytic activity over carbon-supported palladium nanoparticles in dehydrogenation of formic acid. *J. Catal.* **2017**, *352*, 371–381. [CrossRef]
51. Dolas, H.; Sahin, O.; Saka, C.; Demir, H. A new method on producing high surface area activated carbon: The effect of salt on the surface area and the pore size distribution of activated carbon prepared from pistachio shell. *Chem. Eng. J.* **2011**, *166*, 191–197. [CrossRef]
52. Liu, W.J.; Tian, K.; Jiang, H.; Yu, H.Q. Facile synthesis of highly efficient and recyclable magnetic solid acid from biomass waste. *Sci. Rep.* **2013**, *3*, 2419. [CrossRef] [PubMed]
53. Demirbas, A. Effects of temperature and particle size on bio-char yield from pyrolysis of agricultural residues. *J. Anal. Appl. Pyrol.* **2004**, *72*, 243–248. [CrossRef]
54. Schmidt, M.W.I.; Noack, A. Black carbon in soils and sediments: Analysis, distribution, implications, and current challenges. *Glob. Biogeochem. Cycles* **2000**, *14*, 777–793. [CrossRef]
55. Bulushev, D.A.; Zacharska, M.; Shlyakhova, E.V.; Chuvilin, A.L.; Guo, Y.; Beloshapkin, S.; Okotrub, A.V.; Bulusheva, L.G. Single isolated Pd²⁺ Cations Supported on N-doped carbon as active sites for hydrogen production from formic acid decomposition. *ACS Catal.* **2015**, *6*, 681–691. [CrossRef]
56. Jeon, M.; Han, D.J.; Lee, K.S.; Choi, S.H.; Han, J.; Nam, S.W.; Jang, S.C.; Park, H.S.; Yoon, C.W. Electronically modified Pd catalysts supported on N-doped carbon for the dehydrogenation of formic acid. *Int. J. Endocrinol.* **2016**, *41*, 15453–15461. [CrossRef]